

Supporting information

Flexible, environmentally acceptable and long durable energy-efficient novel WS₂- polyacrylamide MOFs for high-performance photodetectors

Arpit Verma¹, Priyanka Chaudhary¹, Ravi Kant Tripathi², B. C. Yadav^{1*}

¹Nanomaterials and Sensors Research Laboratory, Department of Physics,
Babasaheb Bhimrao Ambedkar University, Lucknow-226025, U.P., India

² Department of Physics, Lal Bahadur Shastri Smarak Post Graduate College, Maharajganj-
273161, U.P., India

*Email: balchandra_yadav@rediffmail.com

1. Characterization tools:

Surface morphological analysis was done by JEOL, JSEM- 6490 LV system of Oxford Instruments was and X'Pert Pro PANalytical, Netherland with CuK_α radiation ($\lambda=1.54 \text{ \AA}$) system was used for structural analysis. X-ray photoelectron spectroscopy (XPS) measurements were carried out by Thermofisher Scientific (Model: Nexsa base). Fourier Transform infrared spectroscopic analysis was analyzed by Thermo-Scientific (Nicole 6700) between the ranges of 400-4000 cm⁻¹. Raman analysis was done by Renishaw using 514.5 nm Ar⁺ with a power of 15 mW. The thermogravimetric (TG) and differential thermal (DT) analysis were carried out by the (PERKINELMER STA 6000). For the UV-Visible spectra analysis, a Thermo-Scientific (Evolution 201) spectrophotometer in the range of 190-1100 nm was used. All the photodetection-related measurements were carried out by the Keithley electrometer/ source meter (6517 B) and the illumination intensity was controlled by the Newport optical power meter.

2. Device fabrication and experimental procedure:

Different sequential steps were performed for the preparation of the photodetector device. In the first step, paper substrates were cut in the desired shape and size. 50 mg of the metallopolymeric material was dissolved in 1.5 ml of N-Methyl-2-pyrrolidone ultrasonicated this for 50 min for each samples. This solution was drop-casted on the paper substrate 5 times. These samples were then dried in an oven at 30 °C for 30 min. In the last step, carbon nanotube based electrodes were painted on the substrates with the channel width of 3 mm and length of 1 cm. To examine the photodetector performance time-dependent photoresponse of all three samples carefully examined under illumination intensity of 40 μ W/cm² which centered at a wavelength of 365 nm. All the measurements were carried out in the homemade UV chamber.

3. Structural analysis:

On basis of the X-ray diffractogram, the structural properties of the materials were analyzed. For the WS₂ nanosheet structures Fig. S1(a), as well as the metallopolymer structures different parameters such as Bragg's interplanar spacing, stress, strain and dislocation density, were calculated ¹ and slight changes in these parameters in metallopolymeric nanostructures were observed.

$$2d\sin\theta_{hkl} = n\lambda, \text{ where } n = 1 \quad \text{S (1)}$$

$$\text{Stress } (S) = \frac{\lambda}{L\sin\theta_{hkl}} - \frac{\beta}{\tan\theta_{hkl}} \quad \text{S (2)}$$

$$\text{Strain } (\varepsilon) = \frac{\beta\cos\theta_{hkl}}{4} \quad \text{S (3)}$$

$$\text{Dislocation density } (\delta) = \frac{1}{L^2} \quad \text{S (4)}$$

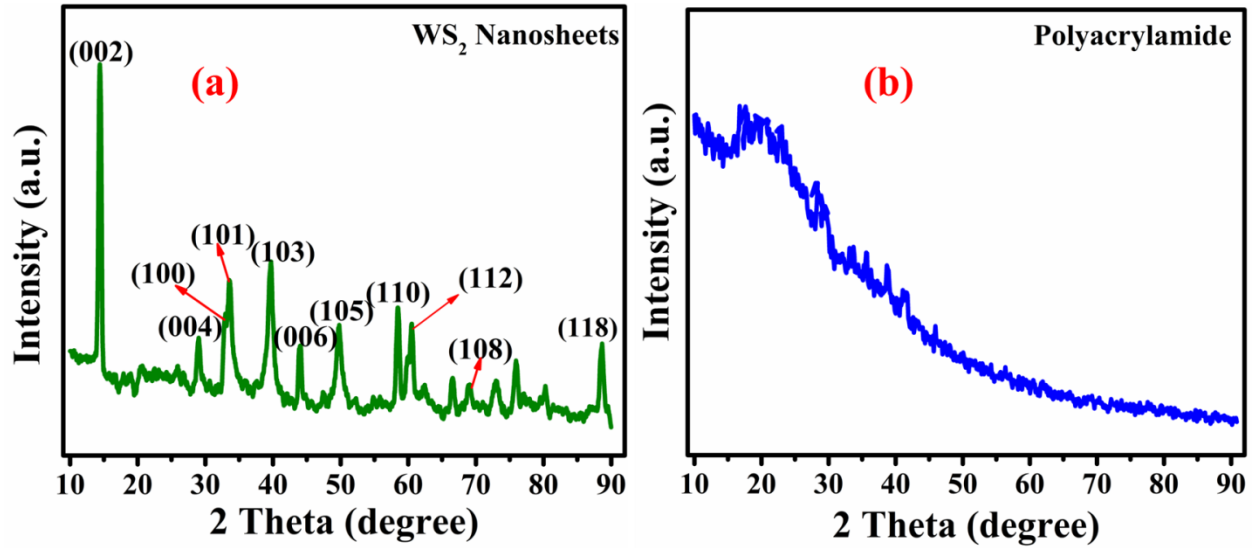


Fig. S1. X-ray diffraction spectra of (a) WS₂ nanosheets (b) frontally polymerized polyacrylamide

As shown in Fig. S2 interplanar spacing and the residual stress present in the as-prepared samples increases as the polymer content increases. The stress and strain generated in the metallopolymeric samples are because different materials possess different expansion coefficients. On increasing the polymer content the polymer strongly capped the WS₂ sheets and larger strains are induced. But strain and the dislocation density decrease with the increasing polymer content. In sample 1, which shows the highest stress among all three samples exhibited the lower photoresponse. The main reason behind this is that stress present in the materials affects the movement of the electrons from one electrode to another electrode. Due to the higher scattering of the electrons, a lower photoresponse was observed in sample 1.²

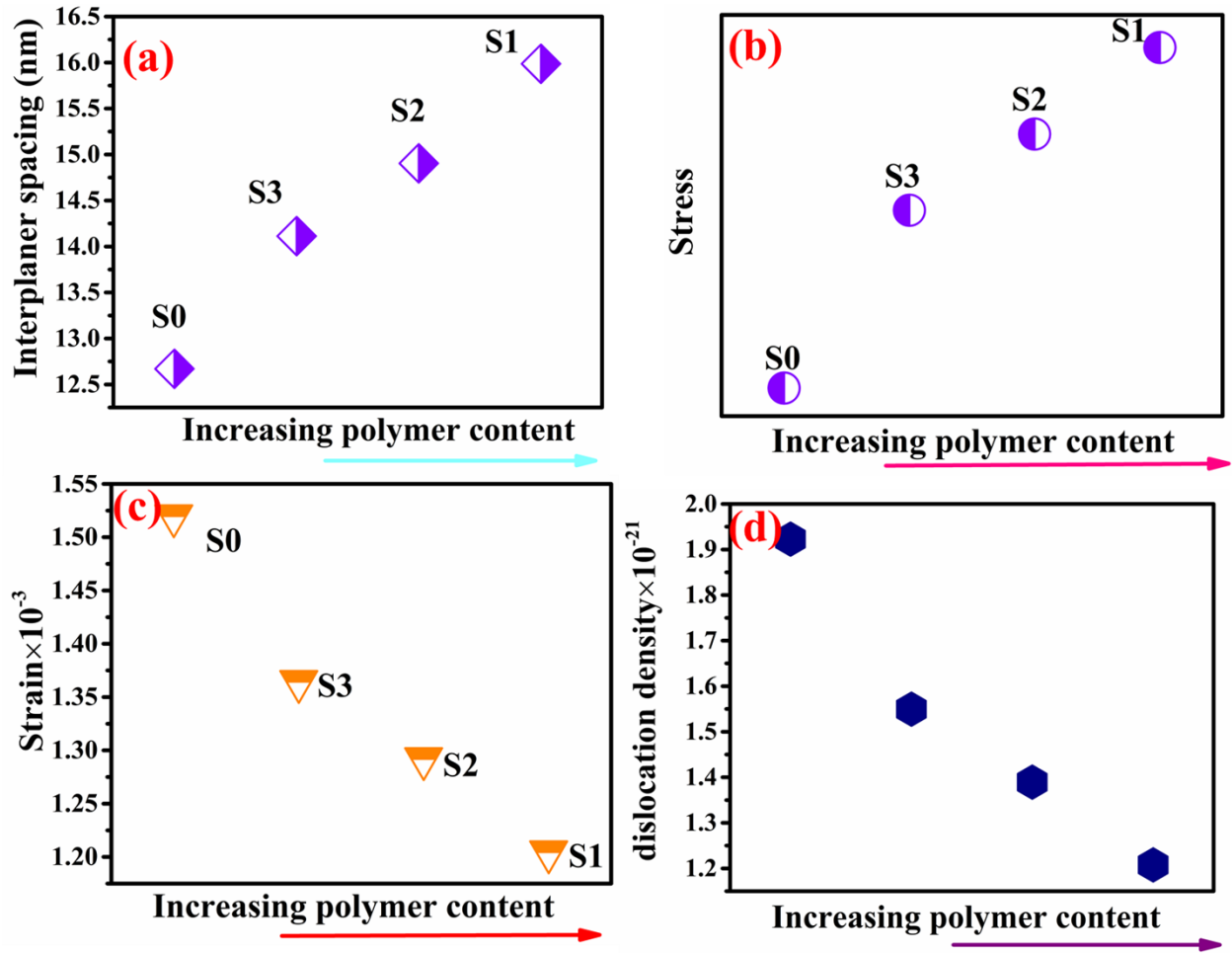


Fig. S2. (a-d) interplanar spacing, stress, strain, and dislocation density respectively

Table S1: structural parameters calculated from the X-ray diffractogram.

Material	2 θ (Deg)	Crystallite size (nm)	FWHM (degree)	Inter-planar spacing d (nm)	Stress (S)	Strain (ϵ) $\times 10^{-3}$	Dislocation density (line/m ³) $\times 10^{15}$
Sample 0 (S0)	14.12516	22.80568	0.34853	12.66967	0.11111012	1.52	1.92
Sample 3(S3)	14.3809	25.40411	0.31288	14.11325	0.11111025	1.36	1.55
Sample 2 (S2)	14.4304	26.82741	0.29628	14.90398	0.11111001	1.29	1.39

Sample 1 14.27134 28.77461 0.27623 15.98577 0.11110974 1.20 1.21
 (S1)

4. FTIR spectra:

In the FTIR spectra of the samples, various peaks are also observed. The peaks observed at 3424.9 cm^{-1} and 3178.1 cm^{-1} are attributed to the asymmetric and symmetric stretching vibrations of the $-\text{NH}_2$ group. Asymmetric vibrations of the $-\text{CH}_2$ functional group is around 2931.2 cm^{-1} . At 1662.3 cm^{-1} peak belongs to $\text{C}=\text{O}$ stretching vibration. C-N stretching vibrations and asymmetric vibrations of the C-C bond are observed at 1405.8 cm^{-1} and 1214.9 cm^{-1} respectively. Bending vibrational peaks of $-\text{NH}_2$ and W-S vibrational peaks are found at 1106.9 and 611.3 cm^{-1} respectively.

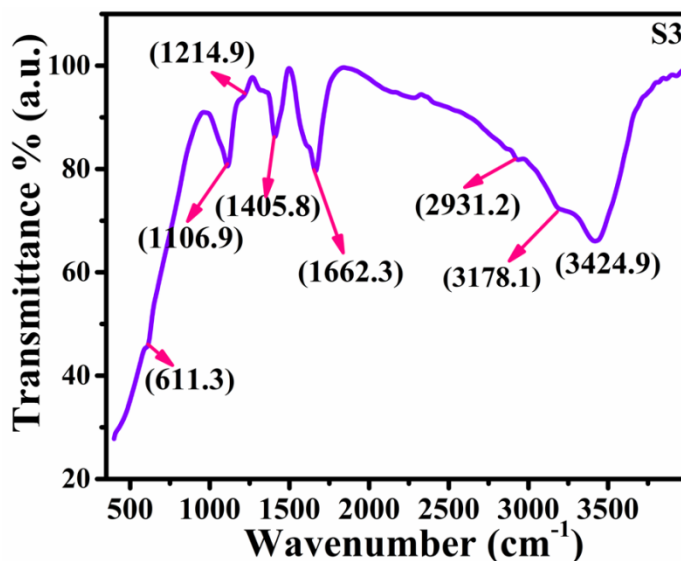


Fig. S3. FTIR spectra of sample 3

Table S2: IR functional groups

S.N.	Peak position (cm^{-1})	Functional group
1.	3424.9	$-\text{NH}_2$ asymmetric vibrations
2.	3178.1	$-\text{NH}_2$ symmetric vibrations

3.	2931.2	-CH ₂ asymmetric vibrations
4.	1662.3	C=O stretching vibrations
5.	1405.8	C-N stretching vibrations
6.	1214.9	C-C vibrations
7.	1106.9	-NH ₂ bending peak
8.	611.3	W-S vibrational peak

5. Conduction mechanism:

Many theories can explain the conductivity in metallopolymers but percolation theory is the most appropriate. WS₂ nanosheets are distributed in an overall polymer matrix, which is more conductive than the polymer matrix. When the concentration of these nanosheets is very small, then inter-particle contact is very small.³ But when a high concentration of the nanosheets is distributed in a polymer matrix and then inter-particle contact is much greater than the lower concentration. Thus the overall conductivity of the higher concentration sample is high. If we add more and more WS₂ nanosheets in the polymer matrix, then the inter-particle contact increases up to a threshold limit, called the percolation threshold.⁴ This theory gives a relationship between direct current conductivity and the concentration of the WS₂ nanosheets by $\sigma_{dc} \propto (p - p_c)^t$, where p and p_c are the WS₂ concentration and percolation, and t is according to model.⁵

In the metallopolymer, some rectangular barriers are formed between the WS₂ nanosheets and polyacrylamide because of the reason that each conduction band of WS₂ and polyacrylamide have different positions. Exponential decay of the wave function in the potential barrier region suggests that tunnelling probability depends on the thickness of the barrier (L). The resistivity of

any tunnel junction is expressed as:

$$\rho_t = \rho_0 \exp\left\{\left(\frac{\pi L}{2}\right) \sqrt{\frac{2mV_0}{\hbar^2}}\right\},$$

where m , V_0 and ρ_0 are the mass of the tunnelling electron, potential barrier height, and resistivity without any barrier. In the metallopolymer nanomaterial, where the tunnelling mechanism dominates there conductivity/resistivity is highly dependent on the separation of the WS₂ nanosheets.⁶ As in this case sample 3 is highly conducting as compared to the 1 and 2. This mechanism of the metallopolymer material is explained based on the current density observed in the samples. As the concentration of the semiconducting WS₂ increases the observed current density also increases. For the S2 sample, the current density of greater than $150 \times 10^{-6} \text{A/cm}^2$ is observed, which is higher than sample 1 and 2. In the solar cell window layer and the photodetector device, many parameters are desirable such as for the solar cell window layer materials high transparency and high conductivity and for the photodetector device, high conductivity and lower dark current is desired properties.⁷ In this material investigation, it is observed that high transparency is obtained in sample 1 but a lower conductivity affects the solar cell efficiency whereas in sample 3 a high conductivity with lower transparency is observed.

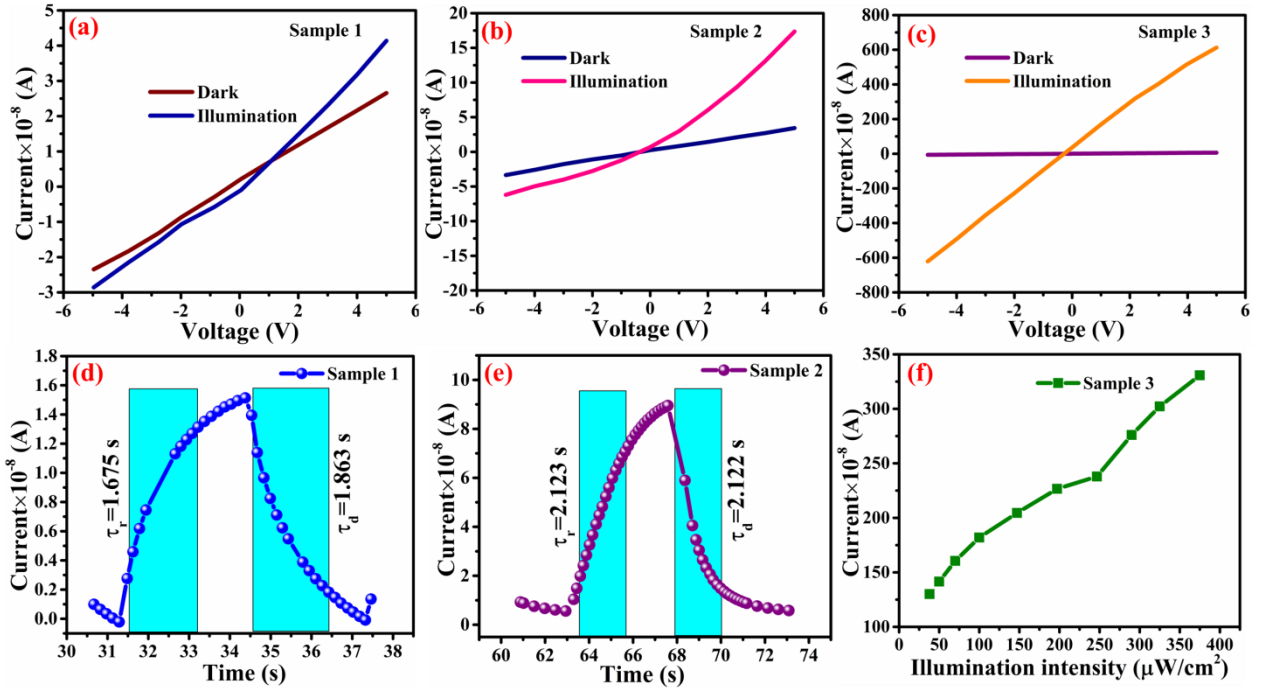


Fig. S4. I-V characteristics of (a) sample 1 (b) sample 2 (c) sample 3, rise and decay curve of (d) sample 1 (e) sample 2 (f) photocurrent at different illumination intensities

6. Photodetector parameters comparison:

For a better understanding and comparison of the metallopolymeric samples, different photodetection parameters are analyzed and presented in Fig. S2. Responsivity, detectivity, linear dynamic range, and the external quantum efficiency of all samples are increasing from sample 1 to 3 as given in Table 2. Thus it can be concluded that on increasing the polymeric content photoresponse are diminished. The reason behind this is that on increasing the polymeric content the distance between the semiconducting WS_2 particulates are increased so the movement of the electrons is disturbed and a lower conductivity is found, which results in poor photodetection parameters.

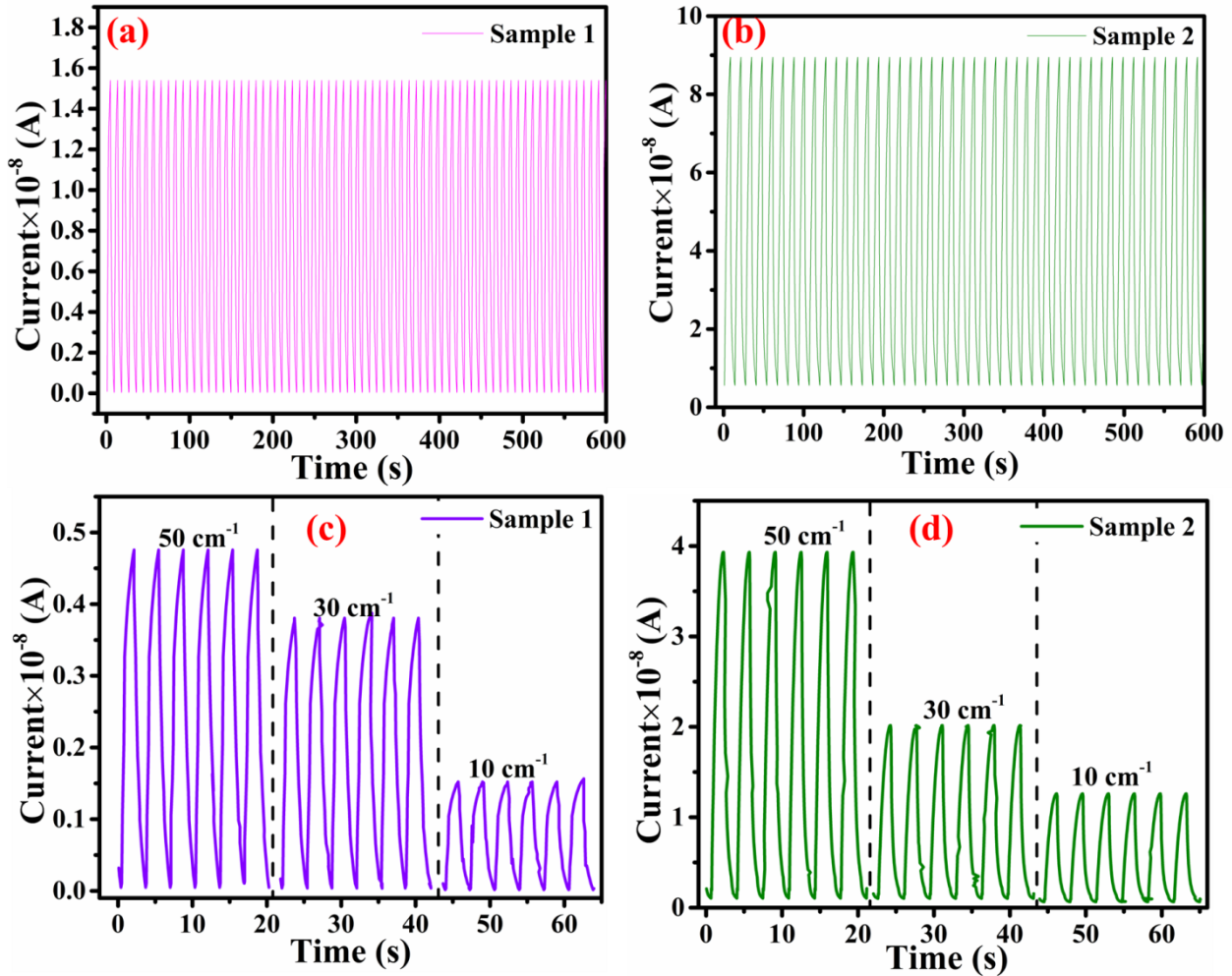


Fig. S5. Stability of (a) sample 2 (b) sample 2, transient photoresponse at different bending curvature of (c) sample 1 (d) sample 2

7. Bending based photoresponse analysis

The flexibility and the durability of the as prepared photodetector devices were investigated. The bending tests of the device fabricated on paper were examined through different bending curvature. The photocurrent results indicate the robustness and stability of the photodetector and its response to the light. From Fig. S5 a and b the long term durability up to 600 s of the photodetector devices are presented whereas in Fig. S5 c and d the flexibility of the devices are

given which indicates the high flexibility of the devices. Photodetector device parameters are given in Table S3 with respect to their bending curvature. In Fig. S6a responsivity with bending curvature of all samples are compared.

Table S3. Different bending curvature based photoresponse

Samples	Responsivity (AW ⁻¹)	EQE (%)	Detectivity (Jones)	NEP (W)	Bending curvature (cm ⁻¹)
Sample 1	0.00476	1.6128	1.1893×10 ¹⁰	2.10×10 ⁻⁶	50
	0.00375	1.2714	9.3750×10 ⁹	2.67×10 ⁻⁶	30
	0.0015	0.5098	3.7593×10 ⁹	6.65×10 ⁻⁶	10
Sample 2	0.0393	13.3311	9.8300×10 ¹⁰	2.54×10 ⁻⁷	50
	0.0199	6.7462	4.9745×10 ¹⁰	5.03×10 ⁻⁷	30
	0.0124	4.1905	3.0900×10 ¹⁰	8.09×10 ⁻⁷	10
Sample 3	0.356	120.8169	8.9088×10 ¹¹	2.81×10 ⁻⁸	50
	0.204	69.0862	5.0943×10 ¹¹	4.91×10 ⁻⁸	30
	0.0365	12.3750	9.1250×10 ¹⁰	2.74×10 ⁻⁷	10

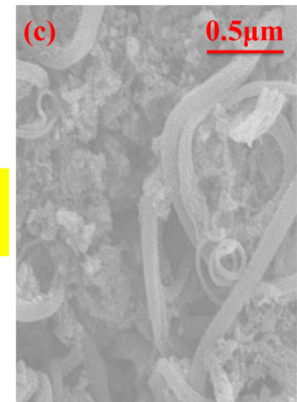
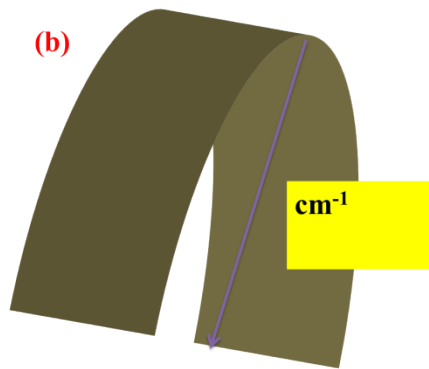
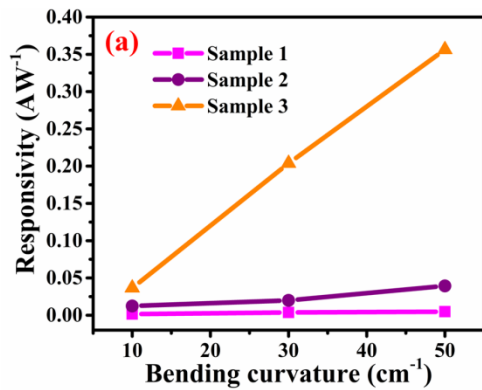


Fig. S6. (a) Responsivity of the all samples at different bending cycles (b) measurement procedure for bending curvature (c) Carbon nanotube image of electrode material

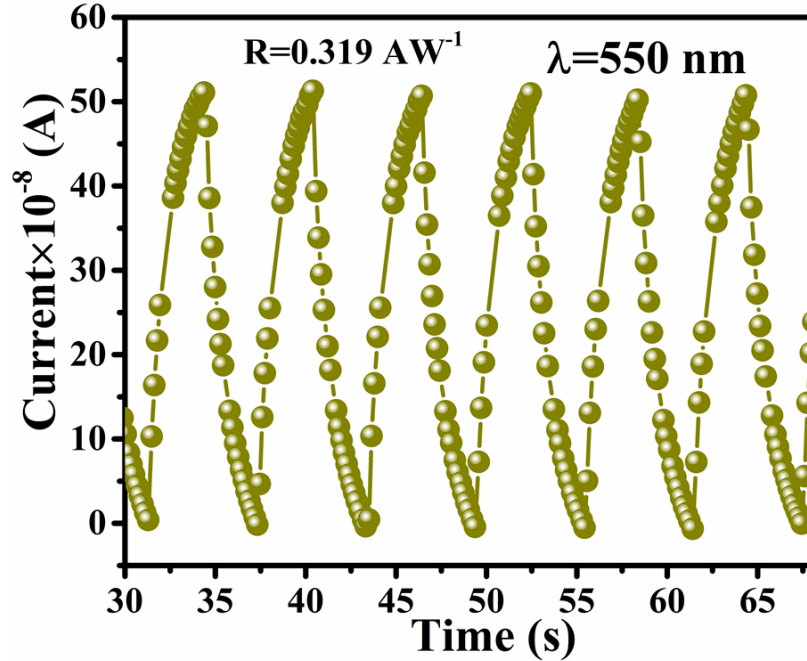


Fig. S7. Photoresponse under the wavelength of 550 nm and optical intensity of $40 \mu\text{W}/\text{cm}^2$.

References:

1. B. D. Cullity, *Elements of X-ray Diffraction*, Addison-Wesley Publishing, 1956.
2. S. Tripathi, B. Kumar and D. K. Dwivedi, *Optik*, 2021, **227**, 166087.
3. J. K. W. Sandler, J. E. Kirk, I. A. Kinloch, M. S. P. Shaffer and A. H. Windle, *Polymer*, 2003, **44**, 5893-5899.
4. J. Li, P. C. Ma, W. S. Chow, C. K. To, B. Z. Tang and J. K. Kim, *Advanced Functional Materials*, 2007, **17**, 3207-3215.
5. L. Wang and Z.-M. Dang, *Applied Physics Letters*, 2005, **87**, 042903.
6. S. H. Foulger, *Journal of Applied Polymer Science*, 1999, **72**, 1573-1582.

7. A. Bouarissa, A. Gueddin, N. Bouarissa and H. Maghraoui-Meherezi, *Materials Science and Engineering: B*, 2021, **263**, 114816.